Seismic interferometry applied to local fracture seismicity recorded at Planchón-Peteroa Volcanic Complex, Argentina-Chile

Casas, J. A.; Draganov, D.; Badi, G. A.; Manassero, M. C.; Olivera Craig, V. H.; Franco Marín, L.; Gómez, M.; Ruigrok, E.

DOI
10.1016/j.jsames.2019.03.012

Publication date
2019

Document Version
Accepted author manuscript

Published in
Journal of South American Earth Sciences

Citation (APA)
Casas, J. A., Draganov, D., Badi, G. A., Manassero, M. C., Olivera Craig, V. H., Franco Marín, L., Gómez, M., & Ruigrok, E. (2019). Seismic interferometry applied to local fracture seismicity recorded at Planchón-Peteroa Volcanic Complex, Argentina-Chile. *Journal of South American Earth Sciences*, *92*, 134-144. https://doi.org/10.1016/j.jsames.2019.03.012

Seismic interferometry applied to regional and teleseismic events recorded at Planchón-Peteroa Volcanic Complex, Argentina-Chile

Casas, José Augusto[a], Draganov, Deyan[b], Badi, Gabriela Alejandra[c], Franco, Luis[d]

[a] *Facultad de Ciencias Astronómicas y Geofísicas, Universidad Nacional de La Plata, CONICET, Argentina*
[b] *Department of Geoscience and Engineering, Delft University of Technology, The Netherlands*
[c] *Facultad de Ciencias Astronómicas y Geofísicas, Universidad Nacional de La Plata, Argentina*
[d] *Observatorio Volcanológico de los Andes del Sur (OVDAS-SERNAGEOMIN), Chile*

Abstract

The Planchón-Peteroa Volcanic Complex (PPVC) is located in the Central Andes, Argentina-Chile. Even though this active volcanic system is considered one of the most dangerous volcano in the region, with more than twenty modest (VEI < 4) Holocene eruptions, knowledge of its subsurface structures, internal processes, dynamics, and their relation, is still limited.

Seismic interferometry (SI) is a high-resolution technique based on analyses of the interference of the propagated seismic energy at one or many stations. SI can be used to characterize the subsurface properties of a target area. In particular, previous SI studies performed in the area of the PPVC describe specific ranges of depth; therefore, more information is required for a thorough description of the subsurface features in the area and for a better understanding of the PPVC dynamics.

We apply SI based on autocorrelations of selected regional and teleseismic events to image the subsurface structures below stations located in

Argentina and Chile during 2012. The selection of the events is performed according to their location, magnitude, angle of incidence of P-wave seismic energy, and signal to noise ratio in the records. For each station, we extract time windows and we process them using three ranges of frequency, which are sensitive to different ranges of depths.

This work describes depths and zones previously not analyzed in the area. The results not only complement the available geological, geochemical, and geophysical information, but present new information for depths between 5 and ∼400 km depth, increasing the general knowledge of the subsurface features in the PPVC. Finally, we also propose a model for the first 45 km of the subsurface (i.e., down to the Moho), which indicates the crustal structure and the likely distribution of magma bodies in depth.

Keywords:
Planchón-Peteroa Volcanic Complex, Seismic Interferometry, Regional and teleseismic events, Magma storage in depth

---

1. Introduction

The Planchón-Peteroa Volcanic Complex -PPVC- (35.223° S, 70.568° W; see location in Figure 1) is located in the Andes at the international border between Argentina and Chile. The PPVC is composed of three main volcanic edifices, i.e., the Azufre, the Planchón, and the Peteroa, out of which the latter is the current active volcano. The PPVC presents overlapped calderas originated from the destruction of several volcanic structures during past explosive events (Tormey, 1989). Through analyses of its historical activity and products, this volcanic system is ranked as the most hazardous volcano in Argentina (Elissondo and Farías, 2016) and the eighth most risky volcano in Chile (Technical sheet, Observatorio Volcanológico de los Andes del Sur, OVDAS-SERNAGEOMIN, Chile).

The knowledge of the PPVC has been developed by the contribution from several disciplines, i.e., geology (Tormey, 1989; Haller et al., 1994; Naranjo et al., 1999; Tapia Silva, 2010; Haller and Risso, 2011), geochemistry (Benavente, 2010; Tassi et al., 2016; Benavente et al., 2016), meteorology (Guzmán et al., 2013), ash analysis (Ramires et al., 2013), seismology (Casas et al., 2014; Manassero et al., 2014; Olivera Craig, 2017; Casas et al., 2018; Casas et al.), gravimetry (Tassara et al., 2006), and risk analysis (Haller and Coscarella). These studies contribute to the knowledge of the eruptive history and the current subsurface conditions of this volcanic system. Nevertheless, the dynamics the PPVC and their relation with the subsurface structures are still poorly understood, increasing the local risk (Elissondo and Farías, 2016).

A description of the subsurface structures (i.e., depth, associated dimensions, density contrasts, etc.) is essential for developing accurate knowledge of the dynamics of any volcanic system. In particular, knowledge of subsurface discontinuities provides constraints for tomographic studies, for magma-ascent modeling, among others, contributing to a better inference of the subsurface conditions, and, therefore, leading to more reliable analyses of likely future volcanic scenarios. Based on structural-geology analyses, Tapia Silva (2010) describes the subsurface geological units located in the very first 10 km of the subsurface in the area of the PPVC, and present their distribution in depth. Even though no local studies have been applied for describing the crustal structure in the PPVC, Farías et al. (2010) and Giambiagi et al. (2012) provide a crustal structure as a function of depth and the distance from the trench in the Central Andes. For the depth of the subducting slab below the PPVC, they estimate four zones delimited in depth at ∼12 (the intracrustal discontinuity), ∼27, and 45 km depth -the crust-mantle discontinuity (the Moho). The Moho is estimated at ∼45 km depth (Tassara et al., 2006); the intra-lithosphere discontinuity (top of lithospheric low-velocity zone), at ∼70 km depth (Karato, 2012); and the top of the subducting slab, at ∼120 km depth (Tassara et al., 2006). Nevertheless, more scientific evidence is required to increase the information about the known subsurface structures, leading to a more accurate characterization of their properties, as well as to describe the subsurface features previously not analyzed. These goals motivate local studies, as the one presented in this article.

Claerbout (1968) has constituted a frame over which the theory of seismic interferometry developed. This passive seismic method -from here on, Seismic Interferometry by Autocorrelations (SIbyA)- suggests that the autocorrelation of a plane-wave transmission response propagating in a horizontally layered medium, recorded at the surface, allows the retrieval of the reflection response of a virtual source co-located to the recording station. SIbyA has shown to be a robust method; it has been applied to different type of seismic data, in several areas and at different scales. For example, SIbyA was applied to global- and teleseismic phases to imaging the crustal subsurface at regional scales (Ruigrok and Wapenaar, 2012; Nishitsuji et al., 2016), to P-wave of microseismic events to imaging the shallow volcanic subsurface (Kim et al., 2017), and to ambient-noise seismic data at several scales (Draganov et al., 2007; Gorbatov et al., 2013; Boullenger et al., 2014; Oren and Nowack, 2017). The robustness of SIbyA has motivated its application to local (Casas et al.), regional, and teleseismic seismic data recorded in the area of the PPVC.

Nishitsuji et al. (2016) apply SIbyA to global seismic phases recorded in the eastern flank of the Peteroa volcano during 2012. They confirm the location of the Moho at ∼45 km depth, and propose a deformation feature in the subducting slab in the form of detachment, shearing, necking, or any combination of them.

Casas et al. apply SIbyA to local seismic events to image the subsurface below the stations located in the Argentine and Chilean sides of the PPVC during 2012. They confirm the geological structure described for the first 4 km of the subsurface (Tapia Silva, 2010), provide information about regions of higher heterogeneity caused by faulting and complex geochemical processes, and support the presence of a magma body emplaced at ∼4 km depth (previously suggested by Benavente (2010)).

We apply SIbyA to regional and teleseismic events selected according to their location, magnitude, angles of incidence of the P-wave seismic energy at each station, and the signal to noise ratio in the records. The results for three different frequency ranges allow the description of the subsurface structures between ∼5 and 400 km depth, and the inference of the crustal structure and the location of magma bodies down to the Moho.

2. Data

The present application uses seismic data recorded by stations deployed in Argentina and Chile during 2012 (see station distribution in Figure 1).

The temporal deployment of seismic instruments in an area of interest is a widely used tool for reaching several goals, e.g., perform first analyses of the propagated wavefield and the subsurface conditions, increase the number of the recording stations, extend the analyzed area, and improve the accuracy of the results. The MalARRgue project (Ruigrok et al., 2012) was designed by institutions from The Netherlands (Delft University of Technology -TUDelft), Argentina (Comisión Nacional de Energía Atómica CNEA), and The United States (Boise State University -BSU). Its goal is imaging and monitoring the subsurface of the Malarge region (Mendoza, Argentina), an area of high scientific interest due to peculiar volcanic and tectonic processes (Stern, 2004). The MarlARRgue project consisted in a temporal deployment (from January 2012 to January 2013) of 38 stations, out of which six were deployed along the eastern flank of the PPVC (from here on, the PV array). The PV array was equipped with short-period (2 Hz) three-component (Sercel L-22) sensors.

Another source of data is provided by three broad-band stations of the Observatorio Volcanológico de los Andes del Sur (OVDAS-SERNAGEOMIN, Chile), which are located ∼6 km northwards. These stations (from here on, OVDAS array) were active during 2012, through the same period as the PV array.

3. Application and results

SIbyA is described by the reciprocity theorem of correlation type (Wapenaar, 2003, 2004). Based on this theorem for transient sources (Wapenaar and Fokkema, 2006), and using autocorrelation in the time domain, we obtain:

$$\sum_{sources} \left\{ \left[T(\mathbf{x_A}, -t) * s_i(-t) * T(\mathbf{x_A}, t) * s_i(t) \right] \otimes \left[s(-t) * s(t) \right]_i \right\} \approx -R(\mathbf{x_A}, -t) + \delta(t) - R(\mathbf{x_A}, t) \quad , \quad (1)$$

which states that the reflection response $R(\mathbf{x_A}, t)$ can be retrieved at the station A located (at $\mathbf{x_A}$) at the surface through the autocorrelation of a recorded transmitted wavefield $T(\mathbf{x_A}, t)$. The operator $*$ indicates convolution, $\otimes$ means deconvolution, and δ is the Dirac's delta. The factor $\left[s(-t) * s(t)\right]_i$ corresponds to the autocorrelated source time function (ASTF), which allows the deconvolution of each source time function $s_i(t)$.

Even though Equation 1 requires sources over the whole stationary phase area (i.e., the Fresnel Zone), seismic events present a non-uniform spatial distribution. Therefore, performing a selection of the seismic sources to be used is essential for a proper application of SIbyA. In order the transmission response of the propagated seismic energy to be accurately estimated by the vertical component of the records, we select only seismic events with P-wave seismic energy arriving (sub) vertically to the station at the surface. The retrieved reflection response (from here on, $R_v(\mathbf{x_A}, t)$) is related to a seismic source co-located to the station at the surface, radiating P-wave energy vertically downwards.

A seismic source in the subsurface release energy that propagates towards the surface in which it is reflected. This seismic energy is reflected, refracted, and diffracted at the subsurface structures and heterogeneities (or the surface), part of which arrives to the recording station at the surface. Seismograms are then composed of direct waves followed by these reverberated waves. SIbyA removes the times previous to the direct arrival, and attenuates the incoherent noise, providing seismic evidence of the location of the subsurface structures. Figure 2 pictures the application of SIbyA in an idealized horizontally layered 2-D medium, given a plane wavefield originated by a seismic source located exactly below the station. The obtained reflection response can be used to know the depth of the reflectors located in the subsurface below the station.

In the real Earth, nor the wave fronts are plane at local and regional scales nor the subsurface is horizontally layered in volcanic zones. In highly heterogeneous zones (as, for example, the area of the PPVC; Manassero et al. (2014)), the location of a seismic source exactly below the station is not an imperative condition for an accurate retrieval of the subsurface reflection response $R_v(\mathbf{x_A}, t)$ (Fan and Snieder, 2009), i.e., the vertical component of the records is still an accurate estimation of the transmission response. Therefore, sources with small P-wave angles of incidence are selected.

3.1. Pre-processing

This section aims to get the input data and prepare it for the proper application of the Equation 1. Using the reference seismic catalogs (IRIS and USGS), we select events occurred during the recording period (i.e., January 2012 until January 2013) and which are characterized by a sufficiently great magnitude so that signal to noise ratio is high in the records of each station. Due to likely variations of the local seismic wavefield in space and time, we judge the signal to noise ratio of each event at each of the stations.

For the selection of seismic events, we use the software JWEED (Java version of Windows Extracted from Event Data) developed by IRIS. Based on restrictions in the origin time, the location, and the magnitude, we preselect events (see Figure 3). According to their epicentral distance, we classify them in two groups. One group is composed of events with epicentral distances between 30° and 120°, and magnitudes greater than Mw. 6; each event of this group guarantees a sufficiently small P-wave ray parameter ($< 0.08\, s/km$) so that seismic energy arrives (sub)vertically at the station, i.e., with incident angles $<\sim 25°$ (Kennett et al., 1995). The second group is composed of events with epicentral distances lower than 30° and magnitudes greater than Mw. 5. These events present a wide range of possible P-wave angles of incidence. Therefore, we perform an examination analysis on this second group in order to select only those events with at least one P-wave phase smaller than the adopted threshold (i.e., $0.08\,s/km$). The ray parameters estimated by the regional velocity model ak135 (Kennett et al., 1995) are appropriate for this analysis, as smaller angles of incidence of the P-wave energy are expected in the real Earth, provided its higher heterogeneity (Fan and Snieder, 2009). Once the seismic events are selected, there is no need to keep the distinction between the groups, i.e., they are equally significant.

The origin time of the selected events is used to extract the seismic waveforms from the records of the PV and OVDAS stations. A first estimate of the P- and S-wave arrival times for each event is calculated using the regional velocity model ak135. These times are then employed to manually pick accurate P- and S-wave arrival times, as well as to get the frequency range of a sufficiently high signal-to-noise ratio. We request a good ($>$ 0.8) signal to noise ratio for the events to be processed, in order to avoid non-interested high amplitudes.

Provided the origin time of the selected events, obtained the accurate arrival times, and examined the (sub)vertical incidence of the P-wave energy and high signal-to-noise ratio of the records, we extract the vertical-component records of the selected events at each of the used stations.

3.2. Processing

The vertical-component records of seismic events with P-wave energy arriving vertically at a station represent an accurate estimate of the P-wave transmission response of such propagated wavefield (provided the discontinuities are not excessively inclined; Nishitsuji et al. (2016)).

Out of the frequency range of processing previously selected for each event according to its signal to noise ratio in the results, we use those frequencies greater than 0.3 Hz, a threshold defined by the instrumental characteristics of the PV-array stations (Nishitsuji et al., 2014). Furthermore, we only use those frequencies shared through the events, i.e., [0.3 2.1] Hz. In order to perform a better interpretation of the results through depth, we segmented this frequency range in two sub-ranges, i.e., [0.3 0.8] Hz and [0.8 2.1] Hz. The separating frequency (0.8 Hz) is selected after a trial and error approach, based on the observed coherency in the results for all the stations in advanced stages of the processing.

In order to avoid the rise of non-physical arrivals caused by cross-terms in the correlations, we extract the times between the first P-wave arrival and the first S-phase arrival. As an example, Figure 4 shows the processing windows for the station PV04, for the complete range of frequencies (i.e., [0.8 2.1] Hz).

The higher value of the selected frequency range (i.e., 2.1 Hz) restricts the resolution of the results for particular depths. Therefore, out of the (previously tested) vertically arriving seismic events, we make a third group composed of those with epicentral distances smaller than 20°. These events are characterized by a sufficiently high signal-to-noise ratio up to 3.2 Hz. As this group aims to provide information about shallower subsurface structures, we select a minimum frequency of 1 Hz. Therefore, we apply the same processing workflow to the three selected frequency ranges, i.e., [0.3 0.8] Hz, [0.8 2.1] Hz, and [1 3.2] Hz. As the same importance is assigned to the events of each of the three groups, we normalize the processing windows according to their vertical flux of seismic energy.

As suggested by Equation 1, we estimate and deconvolve the ASTF from each of the autocorrelated time windows. The ASTF of each event is estimated by the main lobe and the secondary monotonous-decreasing lobes, as shown in Figure 5 for the station AD2 and the frequency range [0.3 0.8] Hz.

Figure 6 presents the autocorrelation of the time windows for the station PV01 and the frequency range [0.3 0.8] Hz, in which each trace is deconvolved by its previously estimated ASTF. This figure shows the dominance of the main lobe in the autocorrelated deconvolved traces. These features close to 0 s are mainly non-physical amplitudes remaining from the deconvolution. Therefore, these amplitudes are removed through windowing.

SIbyA is based on the autocorrelation of time windows extracted from the records of selected seismic events. Note that the autocorrelation of a extracted time window could arise non-physical arrivals at times equal to the time interval between two P-wave arrivals, reducing the quality of the results. However, these time intervals are a function of the epicentral distance of the events. The seismic events used in this application present a wide range of epicentral distances, so that the non-physical arrivals are located at different times in the autocorrelations, leading to a destructive interference of their energy during stacking (see Figure 7).

The last step in the application of Equation 1 is stacking the resulting seismic traces for each station, which enhances the energy from the stationary phase area. Figure 8 shows the pre-stack panel (deconvolved and windowed traces) and the stacked traces for stations AD2 and PV04, for the three selected frequency ranges of processing.

4. Interpretation and discussion

Aiming to compare the seismic results with the known features of the subsurface, we transform the time vector of the results to depth through construction and utilization of a velocity model. This model is composed of velocities provided by the regional model ak135 for depths greater than 60 km, and a modified version of the one obtained by Bohm et al. (2002) for shallower depths (see used velocity model in Figure 9).

Figure 10 and Figure 11 show the stacked traces for the PV and OV-DAS arrays, respectively, for each processing frequency range. These figures also show the interpreted subsurface features for each of the stations. As a complex impedance contrast through depth is expected for the area of the PPVC, we only seek for the dominant amplitudes on the obtained reflection responses, which are potentially related to the main subsurface discontinuities. The lower frequency range (i.e., [0.3 0.8] Hz) leads to describe the subsurface between $\sim$40 and 400 km depth. The results for the other two frequency ranges (i.e., [0.8 2.1] Hz, and [1 3.2] Hz) allow to interpret the subsurface features for depths between 5 and $\sim$45 km. The minimum depth limit is set by the non-physical amplitudes removed from close to 0 s after deconvolution. The maximum depth limit is set by the coherency in the results for all the frequency ranges and all the used stations.

The interpretation of the results for the smallest frequency range ([0.3 0.8] Hz) is performed through contrast of the seismic results and the expected location of the known subsurface features based on the geodynamic scenario and the available geological information for the area of the PPVC (Ferrán and Martínez, 1962; Tassara et al., 2006; Benavente, 2010; Tapia Silva, 2010; Karato, 2012).

The results for the PV array (see Figure 10a) show six dominant amplitudes (i.e., local maximum on the absolute values of the waveforms), which we classify as potential subsurface discontinuities. The close location of the identified features in the seismic results and the known subsurface features lead to the interpretation of the Mohorovicic discontinuity at ∼45 km depth, the intra-lithospheric discontinuity at 65 km, the top of the subducting slab between 110 and 120 km, the bottom of the subducting slab between 140 and ∼160 km, the lithosphere-asthenosphere boundary between 230 and 255 km, and the top of the asthenospheric low-velocity zone between ∼330 and ∼360 km depth.

The OVDAS array (see Figure 11a) is an array located ∼6 km to the north of the PV array, composed of half the stations of the latter, and with greater longitudinal extension. The results for the OVDAS array allow to interpret the Mohorovicic discontinuity at ∼45 km depth, the intra-lithospheric discontinuity between 70 and 90 km, the top of the subducting slab between 115 and 130 km, the bottom of the subducting slab between ∼165 and ∼185 km, the lithosphere-asthenosphere boundary at ∼250 km, and the top of the asthenospheric low-velocity zone between ∼310 and ∼350 km depth.

Based on the seismic velocity values for the depths of interpretation and the frequency range of processing, the resolution of the seismic results is 5 km (Widess, 1973). This value leads to interpret that the results for the OVDAS array do not differ substantially from the results of the PV array, what is expected provided the small geological variation in ∼6 km along the north-south direction for the used processing wavelengths. The best correlation in depth is observed for the Mohorovicic discontinuity (43-48 km depth), the lithosphere-asthenosphere boundary (∼245 km), and the top of the asthenospheric low-velocity zone (∼340 km). A small difference in depth is observed for the intra-lithospheric discontinuity and the top of the subducting slab; even though greater depths are observed in the results of the OVDAS stations, these differences would not be significant based on the vertical resolution of the results. A greater difference is observed for the bottom of the subducting slab, i.e., ∼15 km greater for the OVDAS stations.

Although a dominant positive arrival is expected at the depth of the Moho, a dominant negative amplitude is retrieved in the results for most of the stations. Based on the retrieved waveforms, we interpret the presence of a complex area at ∼40-55 km depth, causing a perturbation of the amplitudes retrieved for these depths, in particular for those related to the Moho.

Even though dipping structures in the subsurface restrict the reflection energy arrived at the surface, we clearly recognize the depth of the top and bottom of the subducting slab. Therefore, two hypotheses arise. One hypothesis suggests a stair-like subduction, according to which the top and the bottom of the oceanic slab present horizontal (or gently inclined) regions; the different depths estimated in the results of the PV and the OVDAS arrays for the bottom of the subducting slab could be caused by a local change of the thickness of the subducting lithosphere. Nevertheless, this hypothesis would not explain the lack of seismicity at the longitude of the stations and depths of analysis (*US Geological Survey*; Nishitsuji et al. (2016)). A second hypothesis (Nishitsuji et al., 2016) proposes a slab deformation in the form of detachment, shearing, necking, or any combination. Then, a differential deformation between the latitudes of the PV and OVDAS arrays would explain the estimated depths for the bottom of the subducting slab. Finally, more information is required to elucidate the proper interpretation.

For the two higher ranges of frequencies (i.e., [0.8 2.1] Hz and [1 3.2] Hz) (see Figure 10b, Figure 10c, Figure 11b, and Figure 11c), the interpretation is also based on the identification of the dominant amplitudes in the results, and the depths for which the arrived reflected energy is particularly smaller, a feature probably caused by the emplacement of a sufficiently great volume of magma as to be manifested in the seismic results.

The results for the PV array and the frequency range [0.8 2.1] Hz (see Figure 10b) indicate five clear dominant arrivals in most of the stations, out of which four are between ∼10 and ∼30 km depth and another one at ∼40 km depth. Additionally, we identify an apparent lack of dominant amplitudes for depths between ∼30 and ∼40 km (indicated with an arrow in Figure 10b). The features identified for [0.8 2.1] Hz are supported by the results for the frequency range [1 3.2] Hz (Figure 10c), which improve the depth of the inferred subsurface discontinuities. In addition, these results manifest an apparent low-amplitude region at ∼25 km depth for the western stations of the array. The results for this frequency range also show a dominant arrival at ∼6 km depth.

The results for the OVDAS stations agree with the interpretation performed for the PV array, for the two analyzed frequency ranges. Therefore, we identify local-maximum amplitudes, as well as apparent small-amplitude zones, at roughly the same depths for the two arrays and for the two higher-frequency ranges, even though the effect of attenuation increases for the highest frequencies (around 3 Hz in this application) (Schön, 2015). Then, these results allow the interpretation of the subsurface structures between 5 and ∼45 km depth (the Moho).

Based on the average depth of the reflectors interpreted in the seismic results, the available scientific information about the subsurface in the PPVC, the proposed structure of the crust for the Central Andes (Farías et al., 2010; Giambiagi et al., 2012), and the physics of magma storage in the crust Jackson et al. (2018), we propose a model for the distribution of magma reservoirs in depth in relation to the main subsurface structures in the crust (see Figure 12).

Through comparison of the average depth of the interpreted reflectors below the stations and the proposed structure of the crust (Farías et al., 2010; Giambiagi et al., 2012), we associate the interpreted reflectors at ∼12, ∼18, and ∼32 km depth as the intra-crustal discontinuity (rigid-ductile discontinuity in the upper crust), the discontinuity between the upper and lower crust, and the rigid-ductile discontinuity in the lower crust, respectively (see Figure 12).

Jackson et al. (2018) models the formation, storage, and chemical differentiation of magma in the Earth's crust. According to the physics of magma storage, the melt fraction is not homogeneously distributed through depth. A great percentage of melt is located in the very upper part of a reservoir, a low percentage is located through most of the reservoir, while a solid area is present in the lower part. The seismic results are most probably evidence of the solid lower section of the reservoir (Jackson et al., 2018). Therefore, we interpret a region in depth as characterized by a magma emplacement in case two conditions are satisfied: 1. the presence of an area of smaller amplitudes in the seismic results, and 2. it is located above any of the interpreted subsurface reflectors. This circumstance is satisfied for two regions, i.e., a shallower zone located above the rigid-ductile discontinuity in the lower crust (i.e., ∼32 km depth); and a deeper one at ∼35 km depth, above a reflector located at ∼40 km.

Even though no amplitude information is available for depths lower than

5 km depth (which are removed after deconvolution), a subsurface model for the area (Benavente, 2010) proposes a magma emplacement at ∼4 km depth. We identify a reflector at ∼6 km depth, which motivates the incorporation of such magma emplacement in our model.

Furthermore, two regions (indicated with a question mark in Figure 12) satisfy only one of the imposed conditions, therefore, their interpretation as regions of magma storage is subjected to extra information. These regions are located above the reflectors interpreted at ∼22 depth and the Moho, for which no apparent smaller amplitudes are observed, probably due to its close location to another feature of the subsurface (upper-lower crust discontinuity and the Moho, respectively), or the resolution of the seismic results are not sufficiently great to recognize a region of limited vertical extension of magma.

Our results support the information obtained for the subsurface in the area (Yuan et al., 2006; Ward et al., 2013; González-Vidal et al., 2018) which indicate (although with a limited resolution) low-velocity zones for approximately the same range of depths. They are also consistent with the conceptual model proposed for the area (Benavente, 2010) for depths between 5 and 15 km depth, for which great volumes of magma storage are not expected.

Finally, more research (e.g., local seismic velocity -or attenuation- tomography studies) is required to accurately identify the location and dimensions of the regions of magma emplacement.

5. Conclusions

Even though the Planchón-Peteroa Volcanic Complex (PPVC) is one of the most hazardous volcanic systems in the Central Andes, knowledge of its internal processes, structures, dynamics, and their relation are still not satisfactorily understood.

We apply seismic interferometry by autocorrelations to regional and teleseismic data recorded by nine stations deployed in the area of the PPVC (six in Argentina and three in Chile) during 2012. The events are selected according their location, magnitude, angle of incidence of the P-wave energy, the signal to noise ratio on the results, and the related useful frequency range. In order to perform an appropriate description of the subsurface structures below the stations, we use three frequency ranges ([0.3 0.8] Hz, [0.8 2.1] Hz, and [1 3.2] Hz) which are sensitive to different range of frequencies.

The smallest frequency range ([0.3 0.8] Hz) is used to infer the tectonic features, i.e., the Moho (at 43-48 km depth), the intra-lithospheric discontinuity ($\sim$70 km), the top and bottom of the subducting slab ($\sim$120 and $\sim$150-165 km), the lithosphere-asthenosphere boundary ($\sim$250 km), and the top of the asthenospheric low-velocity zone ($\sim$340 km). The results support the hypothesis of deformation in the form of detachment, searing, and/or necking for the longitude of the used stations. Our results also suggest a higher depth ($\sim$15 km) for the bottom of the subducting slab at the north of the PPVC, likely caused by differential deformation along the latitude direction.

Based on the results for the two higher-frequency ranges ([0.8 2.1] Hz and [1 3.2] Hz) and previous geological, geochemical, and geophysical information, we propose a model which describes the structure of the crust and the subsurface regions storaging magma bodies down to the Moho. Three regions of sufficiently great volume of magma emplaced at ∼4 km, ∼28 km, and ∼35 km depth, respectively are indicated.

The present work provides valuable information about the subsurface conditions of an active volcanic system -the CVPP. We expect the obtained knowledge to be employed in future research aiming to better understand the dynamics of the CVPP.

References

Benavente, O., 2010. Actividad Hidrotermal asociada a los Complejos Volcánicos Planchón-Peteroa y Descabezado Grande-Quizapu-Cerro Azul, 36S y 37°S, Zona Volcánica Sur, Chile. Universidad de Chile .

Benavente, O., Tassi, F., Reich, M., Aguilera, F., Capecchiacci, F., Gutiérrez, F., Vaselli, O., Rizzo, A., 2016. Chemical and isotopic features of cold and thermal fluids discharged in the Southern Volcanic Zone between 32.5S and 36S: Insights into the physical and chemical processes controlling fluid geochemistry in geothermal systems of Central Chile. Chemical Geology .

Bohm, M., Lüth, S., Echtler, H., Asch, G., Bataille, K., Bruhn, C., Rietbrock, A., Wigger, P., 2002. The Southern Andes between 36 and 40S latitude: Seismicity and average seismic velocities. Tectonophysics .

Boullenger, B., Verdel, A., Paap, B., Thorbecke, J., Draganov, D., 2014. Studying CO 2 storage with ambient-noise seismic interferometry: A combined numerical feasibility study and field-data example for Ketzin, Germany. Geophysics 80, Q1–Q13.

Casas, J.A., Badi, G., Manassero, M., Gomez, P., Draganov, D., Ruzzante, J., 2014. Characterization of Seismo-volcanic Activity in Peteroa Volcano, Central Andes Argentina-Chile. Earth Sciences Research Journal 18, 335–336.

Casas, J.A., Draganov, D., Badi, G., Manassero, M.C., Olivera Craig, V., Franco, L., Gómez, M., Ruigrok, E., . Seismic interferometry applied to local fracture seismicity recorded at Planchón-Peteroa Volcanic Complex, Argentina-Chile. Manuscript under revision .

Casas, J.A., Mikesell, T.D., Draganov, D., Lepore, S., Badi, G.A., Franco, L., Gómez, M., 2018. Shallow S-Wave Velocity Structure from Ambient Seismic Noise at Planchón-Peteroa Volcanic Complex, Argentina-Chile. Bulletin of the Seismological Society of America 108, 2183–2198.

Claerbout, J.F., 1968. Synthesis of a layered medium from its acoustic transmission response. GEOPHYSICS .

Draganov, D.S., Wapenaar, K., Mulder, W., Singer, J., Verdel, A., 2007. Retrieval of reflections from seismic background-noise measurements. Geophysical Research Letters 34.

Elissondo, M., Farías, C., 2016. Volcanic Risk assessment in Argentina, in: Cities on Volcanoes IX, Puerto Varas, Chile.

Fan, Y., Snieder, R., 2009. Required source distribution for interferometry of waves and diffusive fields. Geophysical Journal International 179, 1232–1244.

Farías, M., Comte, D., Charrier, R., Martinod, J., David, C., Tassara, A., Tapia, F., Fock, A., 2010. Crustalscale structural architecture in central

Chile based on seismicity and surface geology: Implications for Andean mountain building. Tectonics 29.

Ferrán, O.L.G., Martínez, M.V., 1962. Reconocimiento geológico de la Cordillera de los Andes entre los paralelos 35 y 38 sur, in: Anales de la Facultad de Ciencias Físicas y Matemáticas, pp. ág–19.

Giambiagi, L., Mescua, J., Bechis, F., Tassara, A., Hoke, G., 2012. Thrust belts of the southern Central Andes: Along-strike variations in shortening, topography, crustal geometry, and denudation. Bulletin of the Geological Society of America .

González-Vidal, D., Obermann, A., Tassara, A., Bataille, K., Lupi, M., 2018. Crustal model of the Southern Central Andes derived from ambient seismic noise Rayleigh-wave tomography. Tectonophysics .

Gorbatov, A., Saygin, E., Kennett, B.L., 2013. Crustal properties from seismic station autocorrelograms. Geophysical Journal International .

Guzmán, C., Hucailuk, C., Tamasi, M., Martínez Bogado, M., Torres, D., 2013. Anomalías Encontradas en los Parámetros Registrados en la Estación de Medición de la Terma del Volcán Peteroa, in: Actas de ICES IX, pp. 186–194.

Haller, M.J., Coscarella, M., . Análisis probabilístico del riesgo de erupción del volcán Peteroa mediante la aplicación de mezcla de distribuciones exponenciales. Nat. Hazards Earth Syst. Sci 9, 425–431.

Haller, M.J., Ostera, H.A., Pesce, A.H., Gardini, M., Folguera, A., 1994. Vulcanoestratigrafía reciente y eruptividad del volcán Peteroa, in: Congreso Geológico Chileno, pp. 319–323.

Haller, M.J., Risso, C., 2011. La erupción del volcán peteroa (3515's, 7018'o) del 4 de septiembre de 2010. Revista de la Asociacion Geologica Argentina .

Jackson, M.D., Blundy, J., Sparks, R.S., 2018. Chemical differentiation, cold storage and remobilization of magma in the Earth's crust.

Karato, S.I., 2012. On the origin of the asthenosphere. Earth and Planetary Science Letters arXiv:1104.0048v2.

Kennett, B.L.N., Engdahl, E.R., Buland, R., 1995. Constraints on seismic velocities in the Earth from traveltimes. Geophysical Journal International .

Kim, D., Brown, L.D., Árnason, K., Ágústsson, K., Blanck, H., 2017. Magma reflection imaging in Krafla, Iceland, using microearthquake sources. Journal of Geophysical Research: Solid Earth .

Manassero, M., Badi, G., Casas, J.A., Gomez, M., Draganov, D., Ruzzante, J., 2014. Seismic attenuation around Peteroa Volcano, Argentina. Earth Sciences Research Journal 18, 341–342.

Naranjo, J.A., Haller, M.J., Ostera, H.A., Pesce, A.H., Sruoga, P., 1999. Geologia y peligros del Complejo Volcánico Planchón-Peteroa, Andes del Sur (3515'S), Región del Maule, Chile-Provincia de Mendoza, Argentina. Servicio Nacional de Geologia y Mineria.

Nishitsuji, Y., Ruigrok, E., Gomez, M., Draganov, D., 2014. Global-phase H/V spectral ratio for delineating the basin in the Malargue Region, Argentina. Seismological Research Letters 85, 1004–1011.

Nishitsuji, Y., Ruigrok, E., Gomez, M., Wapenaar, K., Draganov, D., 2016. Reflection imaging of aseismic zones of the Nazca slab by global-phase seismic interferometry. Interpretation 4, SJ1–SJ16.

Olivera Craig, V., 2017. Relocation of fracture seismicity in Planchón-Peteroa Volcanic Complex through optimization of the arrival-times identification and joint location techniques. Ph.D. thesis.

Oren, C., Nowack, R.L., 2017. Seismic body-wave interferometry using noise autocorrelations for crustal structure. Geophysical Journal International .

Ramires, A., Elissonde, A., Trombotto Liaudat, D., 2013. Posibles escenarios de riesgo frente a la caída de cenizas volcánicas, en el modelo ganadero de la cuenca alta y media del Rio Grande, Malargüe, Mendoza, in: Actas de IX, pp. 304–320.

Ruigrok, E., Draganov, D., Gomez, M., Ruzzante, J., Torres, D., Pumarega, I.L., Barbero, N., Ramires, A., Ganan, A.R.C., van Wijk, K., 2012. Malargüe seismic array: Design and deployment of the temporary array. The European Physical Journal Plus 127, 126.

Ruigrok, E., Wapenaar, K., 2012. Global-phase seismic interferometry unveils P-wave reflectivity below the Himalayas and Tibet. Geophysical Research Letters 39.

Schön, J.H., 2015. Physical properties of rocks: Fundamentals and principles of petrophysics. volume 65. Elsevier.

Stern, C.R., 2004. Active Andean volcanism: its geologic and tectonic setting. Revista geológica de Chile .

Tapia Silva, F.F., 2010. Análisis estructural del sector occidental de la faja plegada y corrida de Malargüe en el curso superior del río Colorado de Lontué (35 18’y 35^{o}23’s), Región del Maule, Chile. Universidad de Chile .

Tassara, A., Götze, H.J., Schmidt, S., Hackney, R., 2006. Three-dimensional density model of the Nazca plate and the Andean continental margin. Journal of Geophysical Research: Solid Earth .

Tassi, F., Aguilera, F., Benavente, O., Paonita, A., Chiodini, G., Caliro, S., Agusto, M., Gutierrez, F., Capaccioni, B., Vaselli, O., Caselli, A., Saltori, O., 2016. Geochemistry of fluid discharges from Peteroa volcano (Argentina-Chile) in 2010-2015: Insights into compositional changes related to the fluid source region(s). Chemical Geology .

Tormey, D., 1989. Geologic history of the active Azufre-Planchon-Peteroa volcanic center (3515’S, Southern Andes) with implications for the development of compositional gaps. Asoc. Gel. Arg. Rev , 420–430.

Wapenaar, K., 2003. Synthesis of an inhomogeneous medium from its acoustic transmission response. GEOPHYSICS .

Wapenaar, K., 2004. Retrieving the elastodynamic Green’s function of an arbitrary inhomogeneous medium by cross correlation. Physical Review Letters 93.

Wapenaar, K., Fokkema, J., 2006. Green’s function representations for seismic interferometry. GEOPHYSICS .

Ward, K.M., Porter, R.C., Zandt, G., Beck, S.L., Wagner, L.S., Minaya, E., Tavera, H., 2013. Ambient noise tomography across the Central Andes. Geophysical Journal International .

Widess, M.B., 1973. How thin is a thin bed? GEOPHYSICS .

Yuan, X., Asch, G., Bataille, K., Bock, G., Bohm, M., Echtler, H., Kind, R., Oncken, O., Wölbern, I., 2006. Deep seismic images of the Southern Andes. Geological Society of America Special Papers .

6. Figures

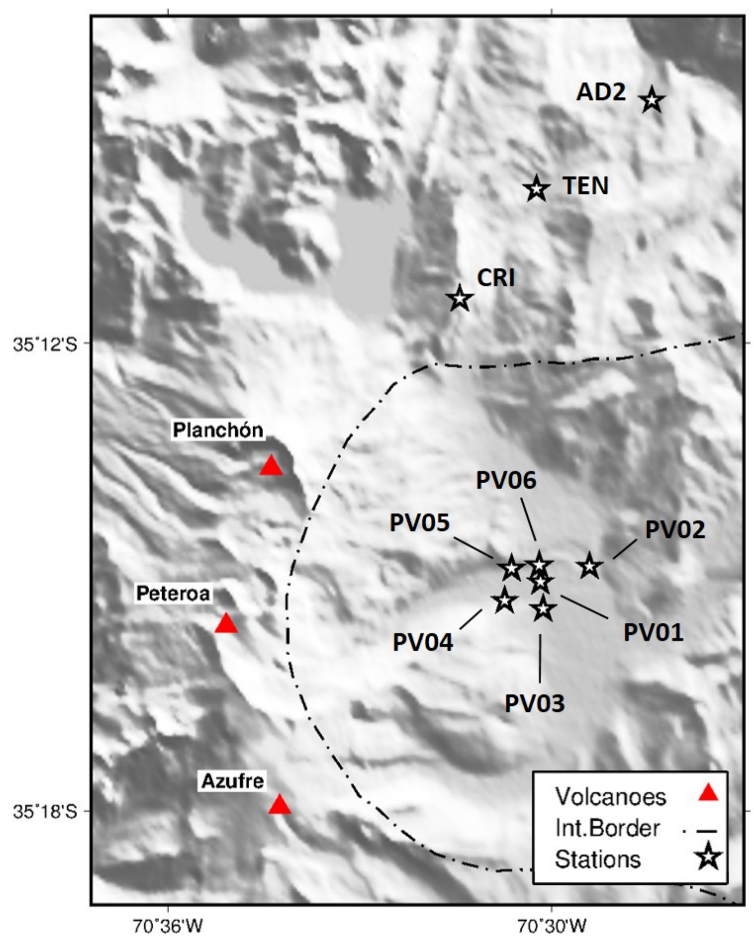

Figure 1: Distribution of the seismic stations used in the present application in relation to the main edifices of the Planchón-Peteroa Volcanic Complex (PPVC).

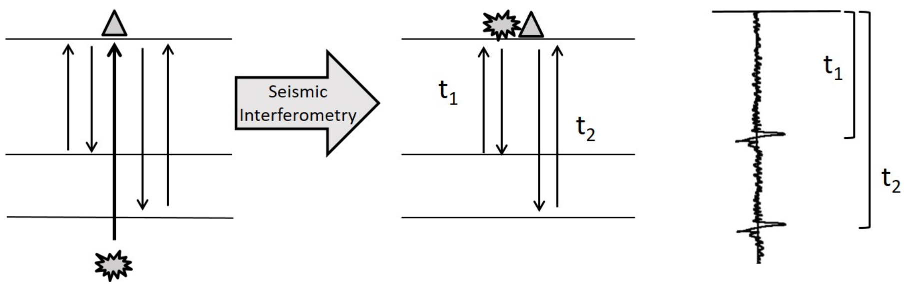

Figure 2: Seismic interferometry by autocorrelation applied to vertically arriving energy in a horizontally layered medium. t_j represents the two-way travel time between the station at the surface and the reflector j in the subsurface. The autocorrelation allows the retrieval of a seismogram composed of reflected energy released by a virtual source co-located at the position of the station.

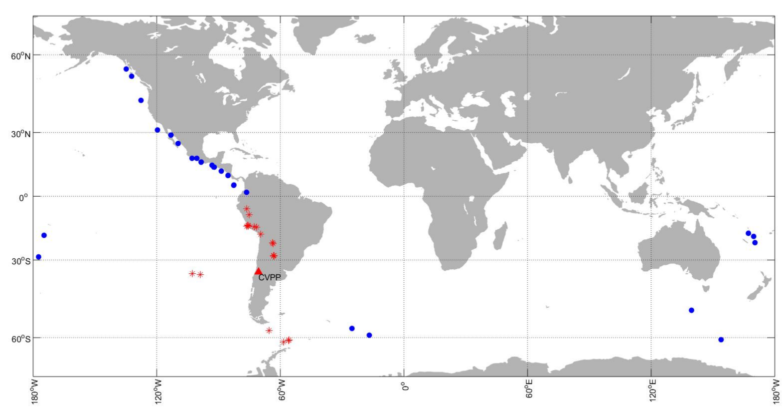

Figure 3: Location of seismic events pre-selected for the application of SIbyA in the area of the PPVC. A triangle indicates the location of the PPVC. Stars show the location of events with epicentral distances less than 30° and magnitudes Mw > 5. Circles indicate events with epicentral distances greater than 30° and less than 120°, and magnitudes Mw > 6.

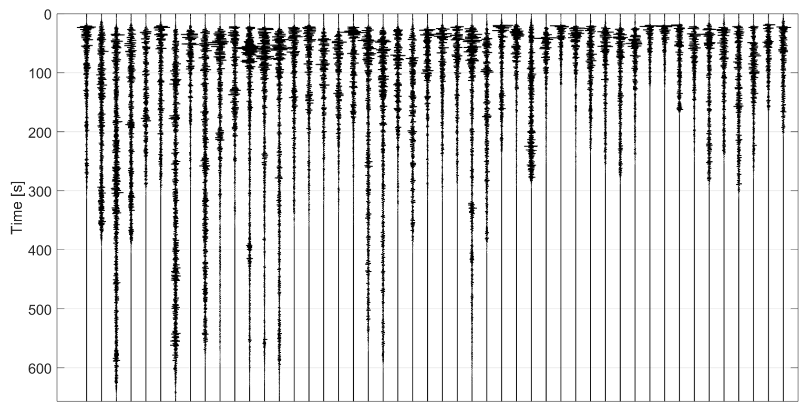

Figure 4: Processing time windows (P-wave codas) for each of the events selected for PV04 station in the complete range of frequencies, i.e., [0.3 2.1] Hz. Each window is normalized according to its vertical energy flux. Vertical axis indicates propagation time. Each window is composed of a pre-event time (20 s) and the times between the first P- and S-wave arrival times.

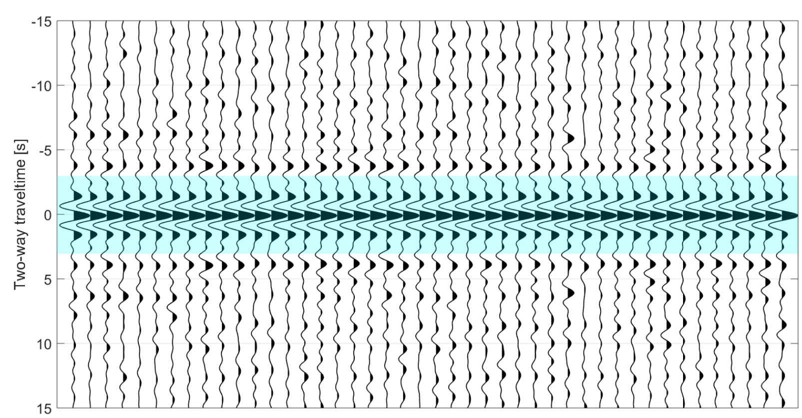

Figure 5: Autocorrelated source time functions (ASTFs) estimated for the station AD2 for the frequency range [0.3 0.8] Hz. A shaded area shows the ASTFs in the autocorrelation panel (for graphical purposes, we only show the first 15 s).

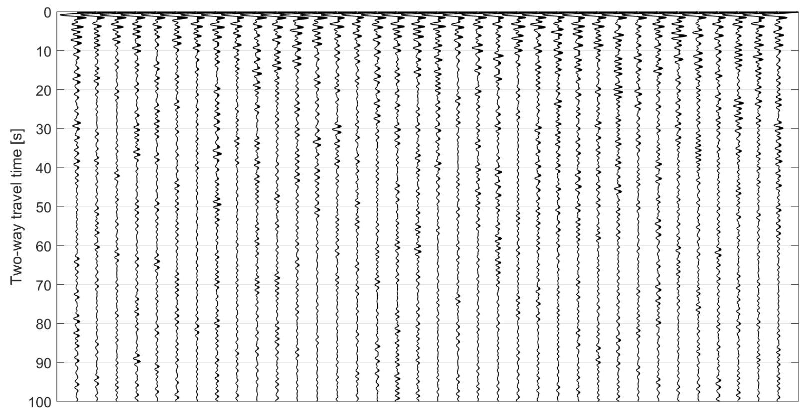

Figure 6: Autocorrelated time windows for the station PV01 in the frequency range [0.3 0.8] Hz. The vertical axis indicates two-way travel time. Each seismic trace is deconvolved by its previously estimated source time function.

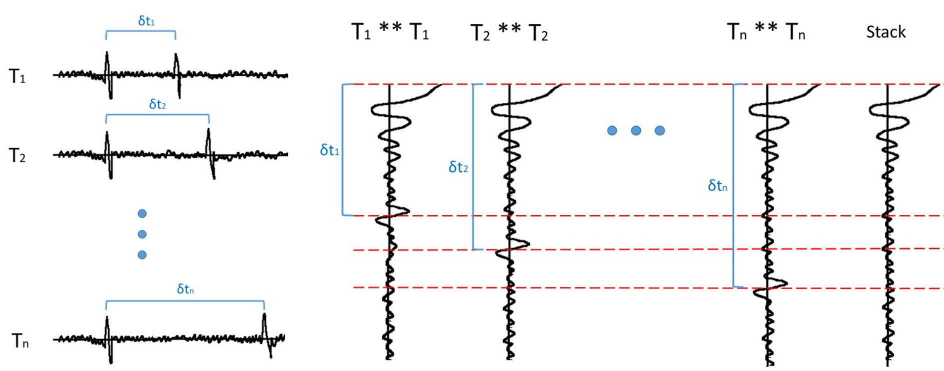

Figure 7: Cartoon illustrating the attenuation of non-physical arrivals originated in the correlation of a time window with several P-wave arrivals. Stacking seismic traces from events with different epicentral distances enhances features located in phase, so that non-physical arrivals due to several P-wave arrivals are attenuated. Without loss of generality, this figure shows the effect of stacking using time windows of events with different epicentral distances, each of them composed of two P-wave phases. T_i is the time window of the event i, which contains two P-wave arrivals separated in δt_i. Operator $**$ means correlation. Dashed lines indicate equal time values.

(a) AD2 [0.3 0.8] Hz

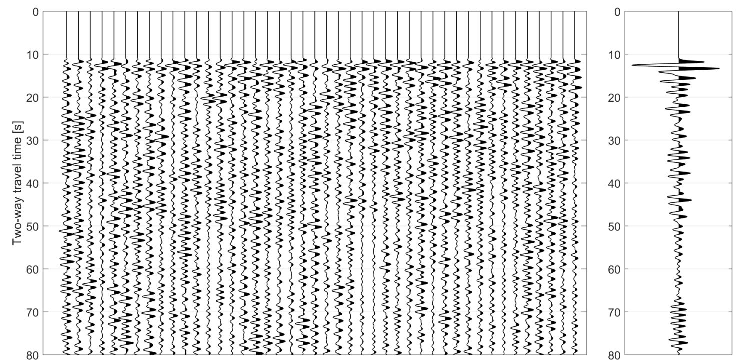

(b) AD2 [0.8 2.1] Hz

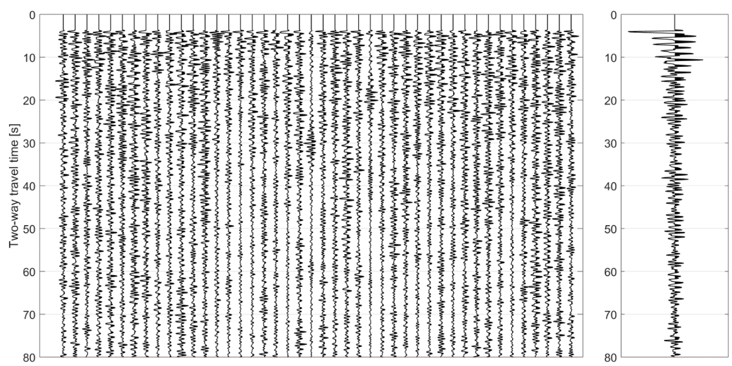

(c) AD2 [1 3.2] Hz

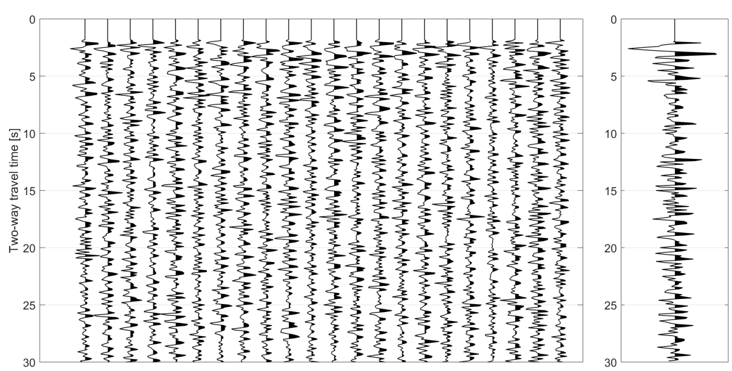

(d) PV04 [0.3 0.8] Hz

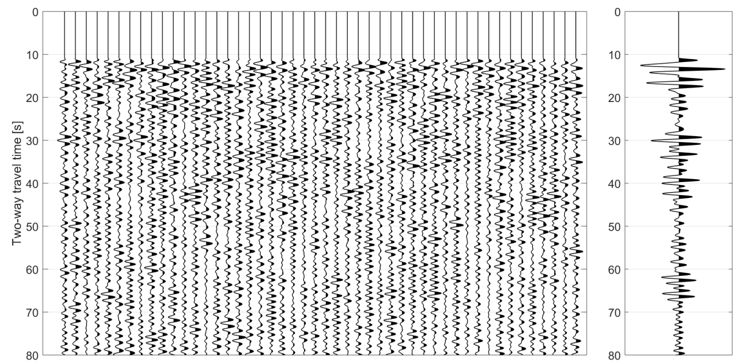

(e) PV04 [0.8 2.1] Hz

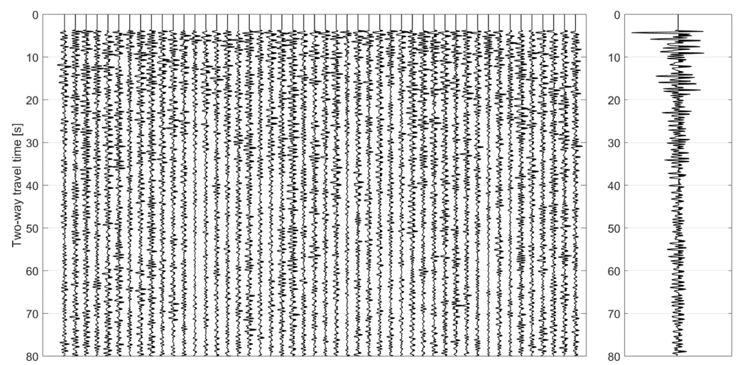

(f) PV04 [1 3.2] Hz

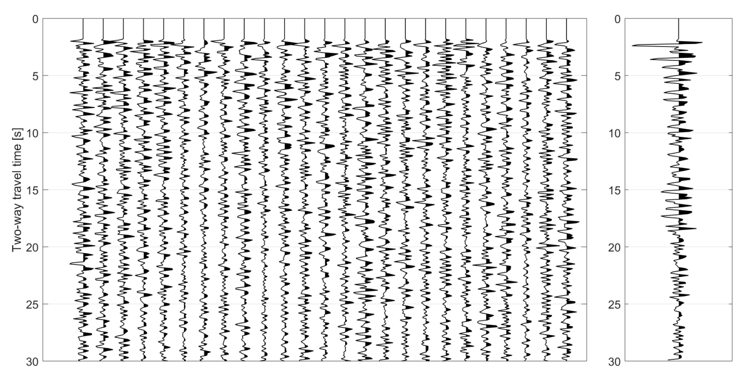

Figure 8: Pre-stacking panels and stacked seismic trace for the stations AD2 (a, b, c) and PV04 (d, e, f), for the frequency ranges [0.3 0.8] Hz (a, d), [0.8 2.1] Hz (b, e), and [1 3.2] Hz (c, f).

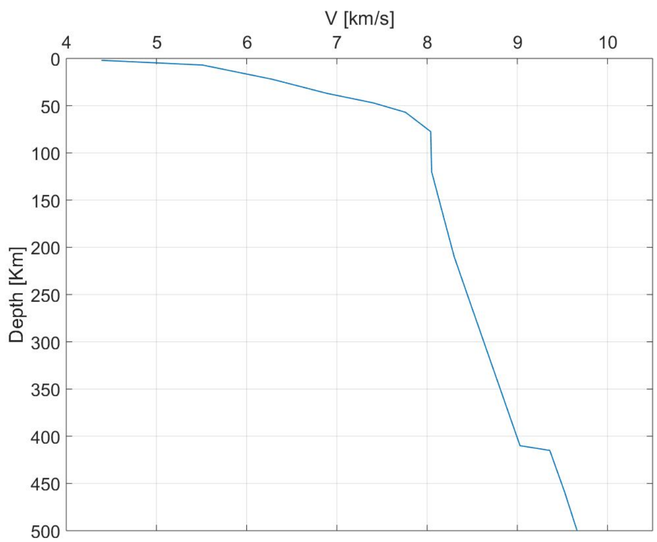

Figure 9: Velocity model used to perform the time-to-depth transformation of the seismic results.

(a)

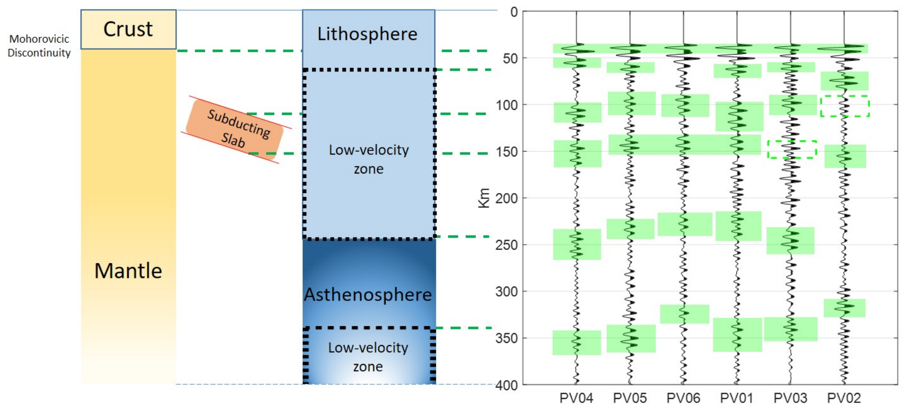

(b)

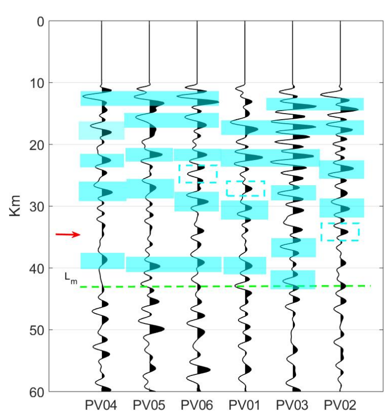

(c)

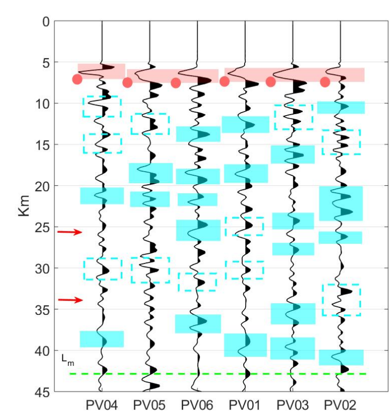

Figure 10: Interpretation of the results at the stations of the PV array for the three frequency ranges: (a) [0.3 0.8] Hz, (b) [0.8 2.1] Hz, y (c) [1 3.2] Hz. Filled rectangle areas show the local maximum amplitudes, i.e., the interpreted subsurface discontinuities below each station. Rectangles with dashed line borders indicate a higher uncertainty at the identification of a discontinuity. Discontinuities interpreted only in (c) are marked with a small circle in the left bottom corner of each rectangle. Figure 10c also shows the interpreted discontinuities at depths close to those interpreted in (b). L_m represent the minimum depth level for the Moho (interpreted in (a)). Arrows indicate zones of likely emplacement of magma.

(a)

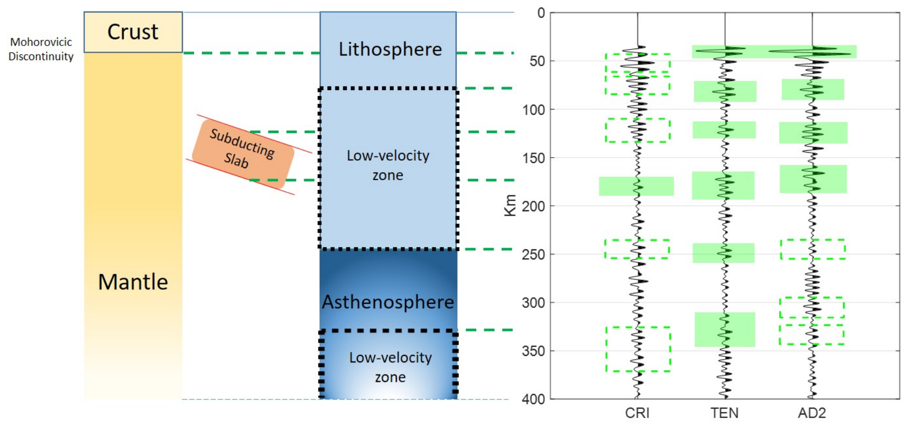

(b)

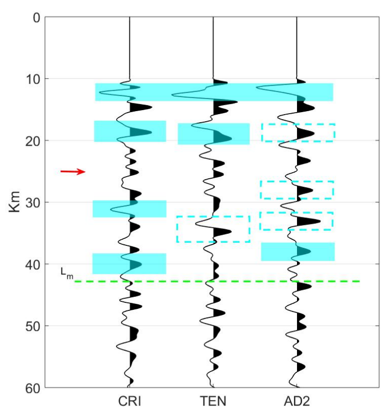

(c)

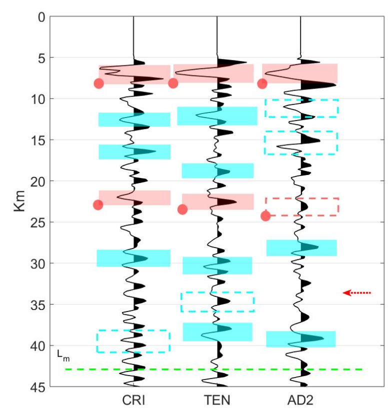

Figure 11: Interpretation of the results at the stations of the OVDAS array for the three frequency ranges: (a) [0.3 0.8] Hz, (b) [0.8 2.1] Hz, y (c) [1 3.2] Hz. Filled rectangle areas show the local maximum amplitudes, i.e., the interpreted subsurface discontinuities below each station. Rectangles with dashed line borders indicate a higher uncertainty at the identification of a discontinuity. Discontinuities interpreted only in (c) are marked with a small circle in the left bottom corner of each rectangle. Figure 11c also shows the interpreted discontinuities at depths close to those interpreted in (b). L_m represent the minimum depth level for the Moho (interpreted in (a)). Arrows indicate zones of likely emplacement of magma. The dashed arrow represents an uncertainty of interpretation higher than in Figure 10.

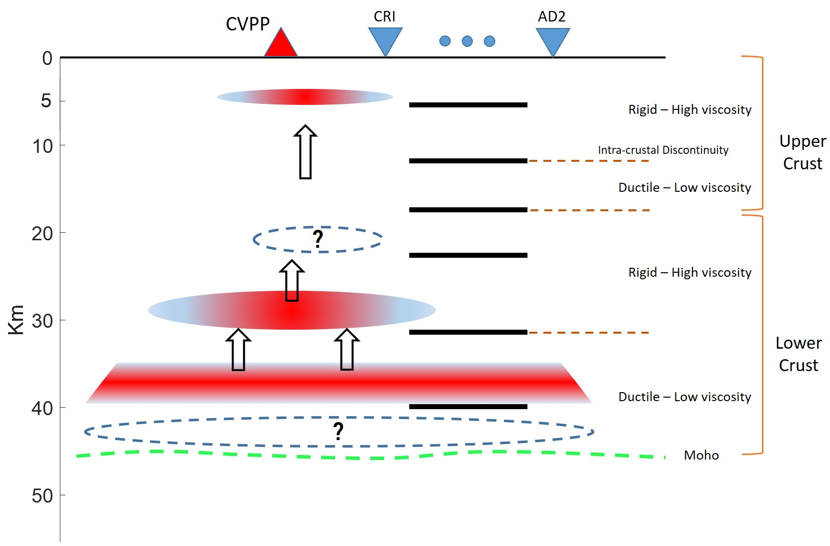

Figure 12: Proposed model of magma emplacement in relation to the structure of the crust down to the Moho in the area of the PPVC. Inverted triangles indicate the longitude of the stations. Thick horizontal lines below the stations show the average depth of the reflectors interpreted in the seismic results. Dashed lines are the interpreted discontinuities (based on Farías et al. (2010) and Giambiagi et al. (2012)) between the different regions of the crust. Arrows show the inferred direction of magma movement. Areas with a question mark inside indicate zones of higher ambiguity in the interpretation.